PEM Fuel Cell Impedance at Open Circuit

A. A. Kulikovsky[a,b,*,z]

[a]*Forschungszentrum Juelich GmbH, Institute of Energy and Climate Research, IEK–3: Electrochemical Process Engineering, D-52425 Jülich, Germany*
[b]*Lomonosov Moscow State University, Research Computing Center, 119991 Moscow, Russia*

A physical model for PEM fuel cell impedance Z at open circuit potential (OCP) is developed and analytical expression for Z is derived. The OCP impedance is a sum of the cathode catalyst layer (CCL) and the gas–diffusion layer (GDL) impedances connected in series. The GDL impedance differs from the Warburg impedance, which is often used in modeling of fuel cell electrodes. A key parameter determining the OCP impedance spectrum is the Newman's dimensionless reaction penetration depth ε. In PEMFCs, ε is large, which makes the GDL impedance a small "invisible" additive to the CCL impedance. In a solid oxide fuel cell (SOFC) anode, ε is small, and the GDL impedance forms a well–resolved separate arc in the impedance spectrum at the OCP. In a real PEM fuel cell, a true OCP regime cannot be achieved due to hydrogen crossover through the membrane. Impedance measurements at zero current in the load yield an equivalent current density of hydrogen crossover through the membrane.
 [DOI: 10.1149/2.0111605jes]

Manuscript submitted October 20, 2015; revised manuscript received January 4, 2016. Published January 15, 2016.

Electrochemical impedance spectroscopy (EIS) provides a unique opportunity for in situ separation of contributions of transport and kinetic processes into a fuel cell potential. This powerful technique continuously attracts new researchers: the Scopus database shows that over the past decade, a number of publications on EIS in chemical engineering has been growing exponentially. At present, literature list on EIS in PEM fuel cells accounts several hundred items; the basic issues are discussed in books of Orazem and Tribollet[27] and Lasia.[22]

In PEMFCs, the anode side impedance is negligible, as the hydrogen diffusivity in the anode porous layers is high, these layers are thin, and the hydrogen oxidation reaction is very fast. The membrane usually gives a trivial ohmic contribution to the cell impedance. Dominating contribution to PEM fuel cell impedance gives the cathode side, a two–layer sandwich formed by the cathode catalyst layer (CCL) and the gas–diffusion layer (GDL). The GDL may contain a thin microporous sub–layer, which improves water management of the cathode side. However, for simplicity we will treat GDL as a single layer with an effective oxygen transport parameter (see below).

PEMFC cathode is a strongly nonlinear system with impedance depending on the working current density j_0. Moreover, the cell transport and kinetic parameters may change with j_0. For deciphering impedance spectra fuel cell developers routinely use the transmission line technique.[1,15,24,26] The largest drawback of this technique is unreliable physical interpretation of the transmission line elements. This explains growing interest in physical models for the PEMFC impedance aiming to determine the basic physical parameters of the cell.[2,4–6,9,11,12,14,25,30–32,35,36] It is worth noting that the numerical impedance models are slow for least–squares fitting of experimental spectra. Analytical models[7,16,19–21] are fast enough for spectra fitting, but they are limited by the cell currents of about 100 mA cm^{-2}.

One of the key cell parameters is the exchange current density i_* of the oxygen reduction reaction (ORR) per unit volume of the electrode. Impedance of the cell operating at a finite current density does not depend on i_*: variation of this parameter simply shifts the polarization curve as a whole along the potential axis, not changing the slope of the curve. In contrast, at the OCP, the CCL impedance depends on i_*.[17] However, the effect of the GDL transport impedance in PEMFC at the OCP yet is not fully understood. To the best of our knowledge, a physical model for the cathode side impedance of a PEMFC at the open circuit potential has not been developed yet.

In solid oxide fuel cell studies, measuring the cell impedance at the OCP is a routine procedure.[3,10,29,33,37] The OCP impedance of a most popular anode–supported SOFC shows two arcs: the high–frequency (HF) charge–transfer arc, and the low–frequency (LF) arc due to hydrogen transport through the porous supporting layer (Figure 1). SOFC anode is a two–layer structure, with a thick ($\simeq$ 0.1 cm) highly porous supporting layer, and a thin ($\simeq$ 10 μm), more dense active layer, where a dominating part of the electrochemical conversion occurs.

In contrast to SOFC, PEMFC impedance at open circuit is rarely measured. Two exceptions are,[34] where the PEMFC impedance at the OCP was measured to determine the ORR exchange current density and,[24] where the OCP impedance of a high–temperature PEM fuel cell was measured to characterize the cell in terms of resistances and capacitances. The Nyquist spectra reported in Refs. 24 and 34 exhibit a single arc (Figures 2, 3).

Basically, each oxygen molecule participating in the ORR must be transported through the GDL, and hence the PEMFC impedance at the OCP must contain a contribution due to oxygen transport in the GDL. Elementary estimate shows that the mass transfer coefficients in a PEMFC cathode and an SOFC anode are of the same order of magnitude. However, the separate low–frequency arc corresponding to the hydrogen transport impedance in SOFC anode is clearly visible in Figure 1, while in the PEMFC cathode spectra, the oxygen transport arc is not seen (Figures 2, 3). What happens to the oxygen transport impedance in a PEM fuel cell at open circuit? The purpose of this work

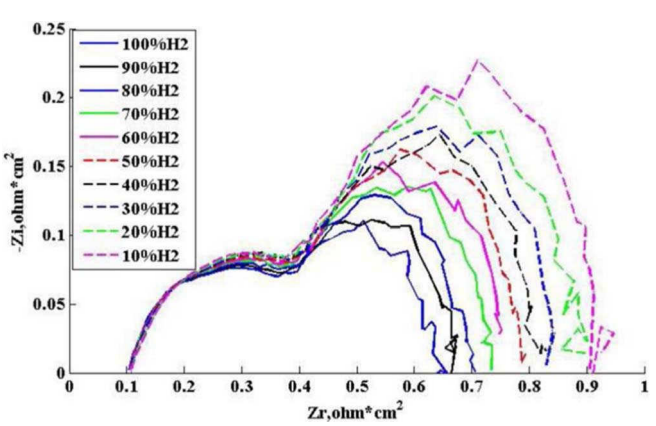

Figure 1. Experimental Nyquist spectra of the anode–supported solid oxide fuel cell at the open–circuit potential for the indicated fraction of hydrogen in the H_2 + H_2O mixture. Reprinted from Ref. 10 with permission of The Electrochemical Society.

*Electrochemical Society Active Member.
[z]E-mail: A.Kulikovsky@fz-juelich.de

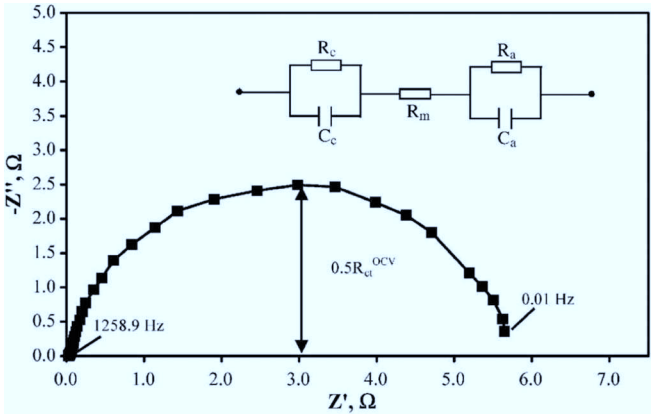

Figure 2. Experimental Nyquist spectrum of the PEM fuel cell at the open–circuit potential. Reprinted from Ref. 34 with permission of Elsevier.

is to calculate the PEMFC impedance at the OCP, and to understand the difference between the OCP impedances of a standard Pt/C–based PEMFC and an anode–supported SOFC.

Model

Cathode catalyst layer.—We will ignore oxygen transport through the CCL. Incorporation of the respective transport equation into the model leads to very cumbersome equations for impedance.[19,20] These equations can be used in numerical fitting algorithms;[19,20] however, they do not help to clarify the physics. Our goal is understanding the relation between the charge–transfer and the GDL–transport impedances and below, we will focus on simple analytical solutions.

The transient CCL model thus includes the proton current conservation Equation 1 and the Ohm's law for the proton transport 2:

$$C_{dl}\frac{\partial \eta}{\partial t}+\frac{\partial j}{\partial x}=-i_*\left[\left(\frac{c_{ox}}{c_{ox}^{ref}}\right)\exp\left(\frac{\alpha F\eta}{RT}\right)-\left(\frac{c_w}{c_w^{ref}}\right)^2\exp\left(-\frac{(1-\alpha)F\eta}{RT}\right)\right] \quad [1]$$

$$j=-\sigma_p\frac{\partial \eta}{\partial x} \quad [2]$$

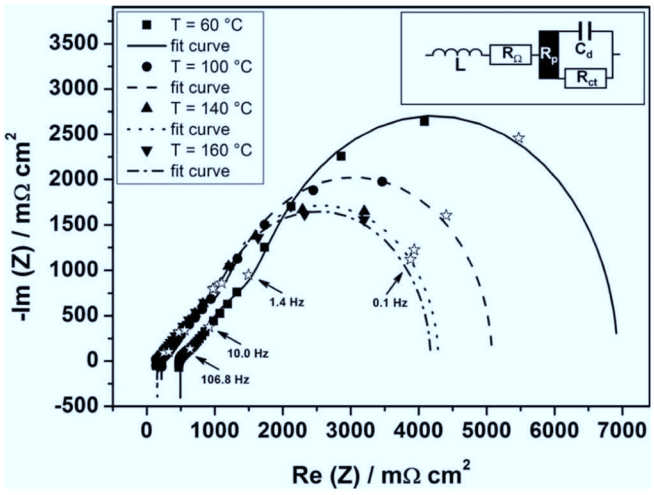

Figure 3. Experimental (points) and fitted transmission line model (lines) spectra of a high–temperature PEM fuel cell for the indicated cell temperatures. Reprinted from Ref. 24 with permission of The Electrochemical Society.

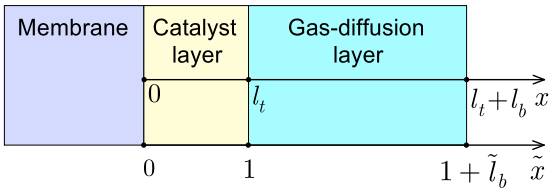

Figure 4. Schematic of the cathode side of a PEM fuel cell and the system of coordinates.

Here x is the distance through the cell (Figure 4), t is time, η is the local ORR overpotential, positive by convention, j is the local proton current density, C_{dl} is the double layer capacitance, i_* is the volumetric exchange current density of the electrode (A cm^{-3}), c_{ox} and c_{ox}^{ref} are the available and reference oxygen concentrations, respectively, c_w and c_w^{ref} are the available and reference water concentrations, respectively, α is the ORR transfer coefficient, and σ_p is the CCL proton conductivity.

The first term on the left side of Eq. 1 describes the charging/discharging of the double layer in the electrode by the proton current. The first exponent on the right side of Eq. 1 describes the rate of proton current consumption in the oxygen reduction reaction (ORR) while the second exponent represents the rate of this current production in the reverse water electrolysis reaction. Detailed discussion of Eq. 1 can be found in Ref. 8, page 406. Below, we will assume that the membrane and the oxygen flow are well–humidified, so that the liquid water concentration in the CCL is close to the reference value.

To simplify calculations, we introduce dimensionless variables

$$\tilde{x}=\frac{x}{l_t},\quad \tilde{t}=\frac{t}{t_*},\quad \tilde{c}=\frac{c}{c^{ref}},\quad \tilde{\eta}=\frac{\eta\alpha}{b_1},\quad \tilde{j}=\frac{jl_t\alpha}{\sigma_p b_1},$$
$$\tilde{l}_b=\frac{l_b}{l_t},\quad \tilde{Z}=\frac{Z\sigma_p}{l_t},\quad \tilde{D}_b=\frac{4FD_bc^{ref}\alpha}{\sigma_p b_1},\quad \tilde{\omega}=\omega t_* \quad [3]$$

where

$$t_*=\frac{C_{dl}b_1}{2i_*\alpha} \quad [4]$$

is the characteristic time of double layer charging. Here and below, the subscript "ox" will be omitted. In Eq. 3, c^{ref} is the oxygen concentration in the channel (reference concentration), l_b is the GDL thickness, l_t is the CCL thickness, ω is the angular frequency of the exciting signal ($\omega=2\pi f$), D_b is the oxygen diffusion coefficient in the GDL, and $b_1=RT/F$ is the characterisitc potential. The subscripts b and t mark the values in the GDL and the CCL, respectively.

Substituting 2 into Eq. 1, setting $c_w=c_w^{ref}$, and using 3, we come to

$$\frac{\partial \tilde{\eta}}{\partial \tilde{t}}-\varepsilon^2\frac{\partial^2\tilde{\eta}}{\partial \tilde{x}^2}=-\frac{1}{2}\left[\tilde{c}\exp(\tilde{\eta})-\exp(-\kappa\tilde{\eta})\right] \quad [5]$$

where

$$\kappa=\frac{1}{\alpha}-1, \quad [6]$$

and ε is the Newman's dimensionless reaction penetration depth:

$$\varepsilon=\sqrt{\frac{\sigma_p b_1}{2i_*l_t^2\alpha}}. \quad [7]$$

This parameter plays a key role in the discussions below. Physically, ε^2 is a ratio of the characteristic current density for ionic (proton) transport in the CCL, $j_p=\sigma_p b_1/(\alpha l_t)$, to the superficial exchange current density of the electrode, $j_*=i_*l_t$. Parameter ε indicates how deeply does the electrochemical reaction penetrate into the electrode due to competition of finite rates of the ORR and ionic transport (see pp 44–54 in Ref. 8 for more detailed discussion).

Linearization and Fourier–transform.—At the OCP, the overpotential $\tilde{\eta}$ is small; it corresponds to the small applied AC perturbation. Expansion of both exponents on the right side of Eq. 5 in series near $\tilde{\eta} = 0$ yields

$$-\left[\tilde{c}\exp(\tilde{\eta}) - \exp(-\kappa\tilde{\eta})\right] \simeq -\left[\tilde{c}(1+\tilde{\eta}) - (1-\kappa\tilde{\eta})\right]$$
$$= -\left[(\tilde{c}-1) + (\tilde{c}+\kappa)\tilde{\eta})\right]$$

and Eq. 5 simplifies to the linear equation

$$\frac{\partial\tilde{\eta}}{\partial\tilde{t}} - \varepsilon^2\frac{\partial^2\tilde{\eta}}{\partial\tilde{x}^2} = -\frac{1}{2}\left[(\tilde{c}-1) + (\tilde{c}+\kappa)\tilde{\eta})\right] \quad [8]$$

At zero current density, the static oxygen concentration equals the reference concentration: $\tilde{c}^0 = 1$. Applying small–amplitude harmonic perturbations

$$\tilde{\eta} = \tilde{\eta}^1\exp(i\tilde{\omega}\tilde{t})$$
$$\tilde{c} = 1 + \tilde{c}^1\exp(i\tilde{\omega}\tilde{t})$$

and neglecting the term with the perturbations product, from Eq. 8 we get a linear equation for the perturbation amplitude $\tilde{\eta}^1$ in the $\tilde{\omega}$–space

$$\varepsilon^2\frac{\partial^2\tilde{\eta}^1}{\partial\tilde{x}^2} = \left(i\tilde{\omega} + \frac{1}{2\alpha}\right)\tilde{\eta}^1 + \frac{\tilde{c}^1}{2}, \quad \tilde{\eta}^1(1) = \tilde{\eta}_1^1, \quad \left.\frac{\partial\tilde{\eta}^1}{\partial\tilde{x}}\right|_{\tilde{x}=1} = 0 \quad [9]$$

Here and below, the superscripts 0 and 1 mark the static solutions and small perturbations, respectively. The first boundary condition in Eq. 9 fixes the applied perturbation of potential $\tilde{\eta}_1^1$ at the CCL/GDL interface. Linearity of Eq. 9 allows us to apply perturbation at either boundary not affecting the solution; for simplicity it is convenient to apply perturbation at $\tilde{x} = 1$. The second boundary condition in Eq. 9 means zero proton current through the CCL/GDL interface.

Eq. 9 contains the perturbation of the oxygen concentration $\tilde{c}^1$ in the CCL. This perturbation must be transported through the gas–diffusion layer, as discussed in the next section.

Oxygen transport in the gas–diffusion layer.—The oxygen transport in the gas–diffusion layer is described by the oxygen mass conservation equation with the Fick's diffusion flux:

$$\frac{\partial c_b}{\partial t} - D_b\frac{\partial^2 c_b}{\partial x^2} = 0 \quad [10]$$

where c_b is the oxygen concentration in the GDL, and D_b is the GDL oxygen diffusivity. As no oxygen is consumed in the GDL, the right side of this equation is zero. Fick's law is a good approximation for oxygen transport in air, where oxygen constitutes a small fraction in the mixture of gases, and in pure oxygen. The coefficient D_b is the effective oxygen diffusion coefficient in the porous media. Generally, this parameter is the oxygen diffusion coefficient in a free space D_{free} corrected by a Bruggemann–type factor for the GDL porosity and tortuosity.

With the dimensionless variables 3, Eq. 10 reads

$$\mu^2\frac{\partial\tilde{c}_b}{\partial\tilde{t}} - \varepsilon^2\tilde{D}_b\frac{\partial^2\tilde{c}_b}{\partial\tilde{x}^2} = 0, \quad [11]$$

where

$$\mu = \sqrt{\frac{4Fc^{ref}\alpha}{C_{dl}b_1}}. \quad [12]$$

Eq. 11 is linear, and hence an equation for the perturbation amplitude $\tilde{c}_b^1(\tilde{x}, \tilde{\omega})$ has the form

$$\varepsilon^2\tilde{D}_b\frac{\partial^2\tilde{c}_b^1}{\partial\tilde{x}^2} = i\tilde{\omega}\mu^2\tilde{c}_b^1, \quad [13]$$

The boundary conditions for Eq. 13 are

$$\tilde{D}_b\left.\frac{\partial\tilde{c}_b^1}{\partial\tilde{x}}\right|_{\tilde{x}=1} = \tilde{j}_0^1, \quad \tilde{c}_b^1(1+\tilde{l}_b) = 0 \quad [14]$$

The first condition relates the oxygen flux at the CCL/GDL interface to the perturbation of the cell current density $\tilde{j}_0^1$ (see below). This condition is consistent with the assumption of fast oxygen transport through the CCL: any perturbation of the proton current density in the membrane immediately induces the change in the oxygen flux at the CCL/GDL interface. The second condition in Eq. 14 means that the oxygen concentration at the GDL/channel interface is fixed and hence the oxygen concentration perturbation is zero at this boundary. Constant oxygen concentration in the channel $c = c^{ref}$ is equivalent to infinite stoichiometry of the air flow.

Continuity of the oxygen concentration at the CCL/GDL interface dictates that

$$\tilde{c}^1 = \tilde{c}_b^1(1) \quad [15]$$

Solutions and impedances.—The system of Equations 9, 13 and the continuity condition 15 describe the total impedance $\tilde{Z}$ of the system "CCL + GDL". The impedance $\tilde{Z}$ is given by the ratio of the cell potential and current density perturbations. The cell potential perturbation equals the overpotential perturbation at the CCL/membrane interface $\tilde{\eta}^1(0)$. From the balance of currents it follows, that the perturbation of electric current at $\tilde{x} = 1$ (Figure 4) equals the perturbation of ionic current at the membrane interface. Using the Ohm's law, the latter perturbation can be expressed as $-\left.\partial\tilde{\eta}^1/\partial\tilde{x}\right|_{\tilde{x}=0}$. Thus, for $\tilde{Z}$ we can write

$$\tilde{Z} = -\left.\frac{\tilde{\eta}^1}{\partial\tilde{\eta}^1/\partial\tilde{x}}\right|_{\tilde{x}=0} \quad [16]$$

Physically, all kinetic and transport processes in a cell, whenever they run, translate into growth of the overpotential $\tilde{\eta}$ and hence this parameter represents the system impedance.

Solution to Eq. 9 reads

$$\tilde{\eta}^1 = \left(\tilde{\eta}_1^1 - \frac{\tilde{c}^1}{2\phi}\right)\cos\left(\frac{\sqrt{\phi}}{\varepsilon}(1-\tilde{x})\right) + \frac{\tilde{c}^1}{2\phi} \quad [17]$$

where

$$\phi = -\frac{1}{2\alpha} - i\tilde{\omega} \quad [18]$$

Solution to the problem 13, 14 is straightforward and it leads to[21]

$$\tilde{c}_b^1(1) = -\frac{\tilde{j}_0^1\tan\left(\mu\tilde{l}_b\sqrt{-i\tilde{\omega}/(\varepsilon^2\tilde{D}_b)}\right)}{\mu\sqrt{-i\tilde{\omega}\tilde{D}_b/\varepsilon^2}} \quad [19]$$

Substitution $\tilde{c}^1 = \tilde{c}_b^1(1)$ into Eq. 17 gives the relation of $\tilde{\eta}^1$ and $\tilde{j}_0^1$. The latter parameter is eliminated using the equation $\tilde{j}_0^1 = -\left.\partial\tilde{\eta}^1/\partial\tilde{x}\right|_{\tilde{x}=0}$. The resulting expression for $\tilde{\eta}^1(\tilde{x})$ is used to calculate the impedance 16, which finally yields

$$\tilde{Z} = -\left[\frac{\sqrt{\phi}}{\varepsilon}\tan\left(\frac{\sqrt{\phi}}{\varepsilon}\right)\right]^{-1} + \frac{\tan\left(\mu\tilde{l}_b\sqrt{-i\tilde{\omega}/(\varepsilon^2\tilde{D}_b)}\right)}{2(1/(2\alpha)+i\tilde{\omega})\mu\sqrt{-i\tilde{\omega}\tilde{D}_b/\varepsilon^2}} \quad [20]$$

The first term on the right side of Eq. 20 is the CCL impedance at the OCP [21]

$$\tilde{Z}_{ccl} = -\left[\frac{\sqrt{\phi}}{\varepsilon}\tan\left(\frac{\sqrt{\phi}}{\varepsilon}\right)\right]^{-1} \quad [21]$$

and the second term is the GDL impedance at the OCP

$$\tilde{Z}_{gdl} = \frac{\tan\left(\mu\tilde{l}_b\sqrt{-i\tilde{\omega}/(\tilde{D}_b\varepsilon^2)}\right)}{2(1/(2\alpha)+i\tilde{\omega})\mu\sqrt{-i\tilde{\omega}\tilde{D}_b/\varepsilon^2}} \quad [22]$$

The GDL impedance differs from the finite–thickness Warburg impedance by the presence of the term $i\tilde{\omega}$ in the factor $2(1/(2\alpha)+i\tilde{\omega})$ in the denominator of Eq. 22. Indeed, omitting $i\tilde{\omega}$ in this factor, we

get the finite–length Warburg impedance $\tilde{Z}_W$ (Ref. 22, page 106):

$$\tilde{Z}_W = \frac{\alpha \tan\left(\mu\tilde{l}_b\sqrt{-i\tilde{\omega}/(\tilde{D}_b\varepsilon^2)}\right)}{\mu\sqrt{-i\tilde{\omega}\tilde{D}_b/\varepsilon^2}} = \frac{\alpha \tanh\left(\mu\tilde{l}_b\sqrt{i\tilde{\omega}/(\tilde{D}_b\varepsilon^2)}\right)}{\mu\sqrt{i\tilde{\omega}\tilde{D}_b/\varepsilon^2}} \quad [23]$$

The relation between $\tilde{Z}_{gdl}$ and $\tilde{Z}_W$ will be discussed in detail in the next section.

Calculating the limit of $\tilde{\omega} \to 0$ in Eqs. 21 and 22, we find the CCL and the GDL static resistivities:

$$\tilde{R}_{ccl} = \frac{\sqrt{2\alpha}\,\varepsilon}{\tanh\left(1/(\sqrt{2\alpha}\,\varepsilon)\right)} \quad [24]$$

$$\tilde{R}_{gdl} = \frac{\alpha\tilde{l}_b}{\tilde{D}_b} \quad [25]$$

In the limits of small and large ε, Eq. 24 transforms to

$$\tilde{R}_{ccl} = \begin{cases} \sqrt{2\alpha}\varepsilon, & \varepsilon \ll 1 \\ \frac{1}{3} + 2\alpha\varepsilon^2, & \varepsilon \gg 1 \end{cases} \quad [26]$$

In dimension form, Eqs. 26 and 25 read

$$R_{ccl} = \begin{cases} \sqrt{\frac{b_1}{i_*\sigma_p}}, & \varepsilon \ll 1 \\ \frac{l_t}{3\sigma_p} + \frac{b_1}{i_* l_t}, & \varepsilon \gg 1 \end{cases} \quad [27]$$

$$R_{gdl} = \frac{b_1}{4FD_b c^{ref}/l_b} \quad [28]$$

and the impedances 21 and 22 read

$$Z_{ccl} = \frac{\sqrt{b_1/(i_*\sigma_p)}}{\sqrt{-1 - i\omega/\omega^*}\tan(\sqrt{(-1 - i\omega/\omega^*)i_* l_t^2/(\sigma_p b_1)})} \quad [29]$$

$$Z_{gdl} = \frac{b_1 \tan\left(\sqrt{-i\omega l_b^2/D_b}\right)}{4Fc^{ref}(1 + i\omega/\omega^*)\sqrt{-i\omega D_b}} \quad [30]$$

where ω^* is the characteristic frequency

$$\omega^* = \frac{i_*}{C_{dl} b_1}. \quad [31]$$

Results and Discussion

PEMFC cathode.—The right side of the GDL static resistivity, Eq. 28 is the ratio of the characteristic potential b_1 to the limiting current density due to oxygen transport in the GDL

$$j_{lim} = \frac{4FD_b c^{ref}}{l_b} \quad [32]$$

Thus, in general, at the OCP, the total system static resistivity $R_{ccl} + R_{gdl}$ "feels" the limiting current density due to oxygen transport in the GDL. However, in PEM fuel cells, the parameter ε is large: $\varepsilon \simeq 10^2$–10^3 (Table I) and the contribution of R_{gdl} appears to be very small. Indeed, for large ε, the CCL resistivity is given by the large–ε part of Eq. 27. The first term on the right side of this equation describes the CCL proton transport resistance, and the second term is the charge–transfer resistance R_{ct}. With the standard cell parameters (Table I), R_{ct} is six orders of magnitude larger than R_{gdl}: $R_{ccl} \simeq R_{ct} \simeq 3{\cdot}10^4\ \Omega\,\mathrm{cm}^2$, while $R_{gdl} \simeq 10^{-2}\ \Omega\,\mathrm{cm}^2$ (Figure 5). Furthermore, due to large ε, the same relation holds for the absolute values of the CCL and GDL impedances

$$|Z_{gdl}| \lesssim 10^{-6}|Z_{ccl}|.$$

In addition, the characteristic frequencies corresponding to the top of the CCL and the GDL arcs (the summit frequencies[29]) are the same, and this finally completely "masks" the GDL impedance by the CCL impedance in PEM fuel cells.

Table I. Typical kinetic and transport parameters of a PEMFC cathode and of an anode–supported SOFC anode. The last four rows indicate the respective dimensionless parameters.

Electrode type	PEMFC cathode	SOFC anode
CL ionic conductivity σ_p, Ω^{-1} cm^{-1}	0.02	0.001, Ref. 33
Volumetric exchange current density i_*, A cm^{-3}	10^{-3}	10^3, Ref. 33
Double layer capacitance C_{dl}, F cm^{-3}	20	2.5, Ref. 33
GDL diffusivity D_b, cm^2 s^{-1}	0.02	0.053, Ref. 10
Catalyst layer thickness l_t, cm	0.001	0.002
GDL thickness l_b, cm	0.02	0.15, Ref. 10
Transfer coefficient α	1	0.5
Pressure p, atm	1 (air)	0.1 H_2 + 0.9H_2O
Cell temperature, K	273+70	273 + 700
Tafel slope b, mV	29.55	168
Feed molecules molar concentration in the channel c^{ref}, mol cm^{-3}	$7.36 \cdot 10^{-6}$	$1.24 \cdot 10^{-5}$
ε	547.7	0.145
$\tilde{D}_b$	77.2	151
$\tilde{l}_b$	20	75
μ	1.97	1.07

To prove these statements we perform asymptotic expansions of impedances 21 and 22 over large ε:

$$\tilde{Z}_{ccl} \simeq \frac{1}{3} + \frac{\varepsilon^2}{i\tilde{\omega} + 1/(2\alpha)} + O(\varepsilon^{-2}), \quad \varepsilon \to \infty \quad [33]$$

$$\tilde{Z}_{gdl} \simeq \frac{\tilde{l}_b}{2\tilde{D}_b(i\tilde{\omega} + 1/(2\alpha))} + O(\varepsilon^{-2}), \quad \varepsilon \to \infty \quad [34]$$

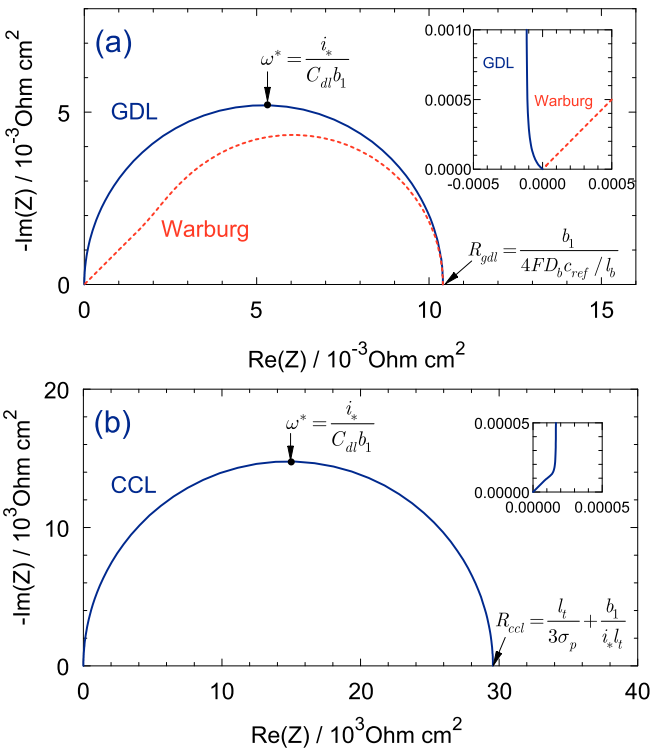

Figure 5. Model Nyquist spectra of a PEMFC: (a) GDL impedance, and (b) CCL impedance. The total impedance of the system "CCL+GDL" is indistinguishable with the CCL impedance in (b) (see text). Insets show the high–frequency parts of the spectra. Note quite a significant difference of the GDL impedance from the classic finite–thickness Warburg impedance.

At the top point of the respective arc, the following relation holds: $\partial\,\mathrm{Im}\,(\tilde{Z})/\partial\tilde{\omega} = 0$. Equating the $\tilde{\omega}$–derivatives of the imaginary parts of Eqs. 33 and 34 to zero, and solving the resulting equations for $\tilde{\omega}$, we get the summit frequencies $\tilde{\omega}^*_{ccl}$ and $\tilde{\omega}^*_{gdl}$

$$\tilde{\omega}^*_{ccl} = \tilde{\omega}^*_{gdl} = \frac{1}{2\alpha}, \quad \text{or} \quad \omega^*_{ccl} = \omega^*_{gdl} = \omega^* = \frac{i_*}{C_{dl} b_1} \qquad [35]$$

Thus, the summit frequency of the CCL and GDL arcs coincide. This means, that these arcs almost completely merge, except in the high–frequency range.

In dimension form, Eqs. 33, 34 read

$$Z_{ccl} \simeq \frac{l_t}{3\sigma_p} + \frac{b_1}{i_* l_t (1 + i\omega/\omega^*)} \qquad [36]$$

$$Z_{gdl} \simeq \frac{l_b b_1}{4F D_b c^{ref} (1 + i\omega/\omega^*)} \qquad [37]$$

where ω^* is given by Eq. 35. Eqs. 36, 37 lead to the static resistivities given by Eqs. 27 and 28, respectively. However, in the high–frequency limit, the accuracy of Eqs. 36, 37 progressively worsens with the growth of ω. At large $\tilde{\omega}$, the absolute value of the first truncated term in the expansion 33 is $\tilde{\omega}/(45\varepsilon^2)$, i.e., Eqs. 33, 36 are accurate up to the frequency satisfying to

$$\tilde{\omega} \ll 45\varepsilon^2, \quad \text{or} \quad \omega \ll \frac{45\sigma_p}{l_t^2 C_{dl}} \simeq 4.5 \cdot 10^4 \ \mathrm{s}^{-1} \qquad [38]$$

Quite similar analysis of truncated terms leads to the following condition of validity of Eqs. 34 and 37

$$\tilde{\omega} \ll \frac{15\tilde{D}_b^3\varepsilon^4}{\mu^4 \tilde{l}_b^5}, \quad \text{or} \quad \omega \ll \frac{30 C_{dl} l_t F D_b^3 c^{ref}}{l_b^5 \sigma_p i_*} \simeq 5.3 \cdot 10^7 \ \mathrm{s}^{-1} \qquad [39]$$

Thus, Eqs. 33, 34 and their dimension versions 36, 37 are valid for the regular frequencies f below 1 kHz.

Neglecting the small term 1/3 in Eq. 33, and dividing this equation by Eq. 34, we get

$$\frac{\tilde{Z}_{ccl}}{\tilde{Z}_{gdl}} \simeq \frac{2\tilde{D}_b\varepsilon^2}{\tilde{l}_b} = \frac{j_{lim}}{i_* l_t} \simeq 2.8 \cdot 10^6 \qquad [40]$$

where j_{lim} is given by Eq. 32. Thus, in the frequency range given by Eq. 38, the CCL impedance exceeds the GDL impedance by six orders of magnitude.

Six orders of magnitude smaller than Z_{ccl} impedance is hardly measurable. Theoretically, Z_{gdl} can be measured using the following technique. Eqs. 37 and 36 show that Z_{gdl} is inversely proportional to the channel oxygen concentration c^{ref}, while Z_{ccl} is independent of this parameter. Thus, in principle, we can mesure the total cell impedance $Z_{ccl} + Z_{gdl}$ for two oxygen concentrations, e.g., for the concentration in air c_a and in pure oxygen c_o. In this way, we get two spectra $Z_{ccl} + Z^a_{gdl}$ and $Z_{ccl} + Z^o_{gdl}$. Subtracting one from another, in accordance with 37 we get the spectrum Z^{a-o}_{gdl}, which does not contain large Z_{ccl}:

$$Z^{a-o}_{gdl} = \frac{l_b b_1}{4F D_b (1 + i\omega/\omega^*)} \left(\frac{1}{c_a} - \frac{1}{c_o} \right)$$

Fitting this equation to the experimental points, we could determine the oxygen diffusion coefficient in the GDL, D_b. However, both the spectra $Z_{ccl} + Z^a_{gdl}$ and $Z_{ccl} + Z^o_{gdl}$ must be measured with at least eight significant digits. With the present state of experimental technique such measurements seem to be difficult, if not impossible.

SOFC anode.—In SOFC anode, the dominating part of ionic current is converted in the thin anode functional layer, i.e., the fraction of current converted in the thick supporting layer is vanishingly small.[38] This allows us to consider the supporting layer of SOFC anode as an analog of the gas–diffusion layer in PEMFCs, and to apply the model above to the anode–supported SOFC anode. The system of Equations 1, 2, 10 remains the same, with the obvious change of the oxygen concentration to the hydrogen concentration in Eqs. 1 and 10. Note that in this section, D_b in Eq. 10 is the hydrogen diffusion coefficient in the supporting layer, and the fraction of H_2 in the $H_2 + H_2O$ mixture feeding the anode is assumed to be small.

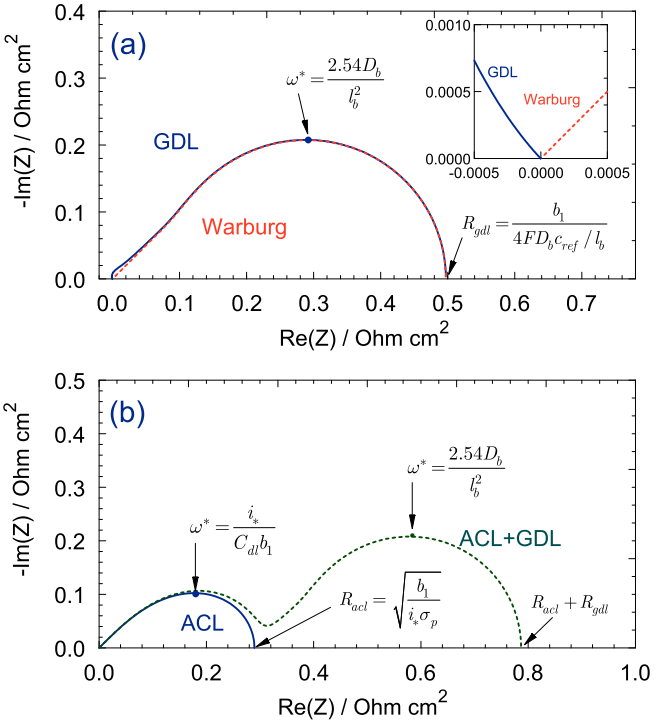

Figure 6. The same as in Figure 5 for the anode of the anode–supported solid oxide fuel cell. Here, GDL stands for the supporting layer of the anode, the ACL indicates the thin anode catalyst (functional) layer, and σ_p is the ionic conductivity of the ACL. Note that the GDL impedance is close to the finite–thickness Warburg impedance.

A key feature of this electrode is a large value of the exchange current density, which makes the parameter ε small: $\varepsilon \ll 1$ (Table I). A typical operating temperature of SOFC is about 273 + 700 K; an Arrhenius–type dependence of i_* on temperature makes the value of i_* in an SOFC anode six orders of magnitude larger, than i_* in a PEMFC cathode. The impedance spectrum of a small–ε SOFC anode drastically differs from impedance of a large–ε PEMFC cathode.

Figure 6a shows the anode support (GDL) impedance, and Figure 6b depicts the anode catalyst layer (ACL) impedance and the total SOFC anode impedance. These curves are calculated using Eqs. 30, 29, and the data in the last column in Table I. The ACL and the GDL impedances are represented by the well–separated arcs (Figure 6b, cf. Figure 1). Note that the GDL impedance is close to the Warburg impedance (Figure 6a).

Figure 6 suggests, that the small–ε GDL impedance differs from the Warburg impedance at high frequencies only. To show this, we calculate the real and imaginary parts of the leading term in the Taylor series expansion of Eq. 22 over ε at $\varepsilon = 0$ (Appendix):

$$\tilde{Z}_{gdl,re} = \frac{\alpha(1 - 2\alpha\tilde{\omega})\varepsilon}{\mu\sqrt{\tilde{\omega}\tilde{D}_b}(1 + 4\alpha^2\tilde{\omega}^2)} \qquad [41]$$

$$\tilde{Z}_{gdl,im} = -\frac{\alpha(1 + 2\alpha\tilde{\omega})\varepsilon}{\mu\sqrt{\tilde{\omega}\tilde{D}_b}(1 + 4\alpha^2\tilde{\omega}^2)} \qquad [42]$$

Note that this expansion is valid at high frequencies only, when $\varepsilon^2/\tilde{\omega} \ll 1$. The Nyquist plot of Eqs. 41, 42 differs from the Warburg 45°–slope straight line at high frequencies only (Figure 7). The spectrum 41, 42 exhibits a curved arc located in the HF domain (Figure 7). With the decrease in ε, the scale of the Figure 7 decreases,

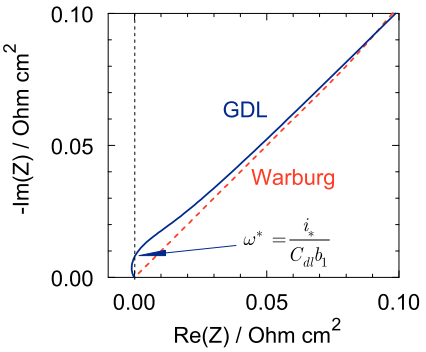

Figure 7. GDL impedance, Eq. 22 in the limit of $\varepsilon \to 0$, Eqs. 41, 42. The characteristic frequency, where the real part of impedance becomes negative is $i_*/(C_{dl} b_1)$. Parameters for the calculations are shown in the last column of Table I.

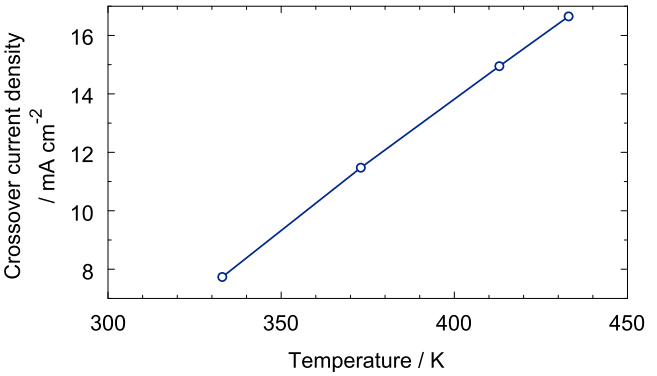

Figure 8. Temperature dependence of the equivalent current density of hydrogen crossover through the membrane in a high–temperature PEMFC. The plot is obtained using the model above and the data from Ref. 24.

as $\tilde{Z}_{gdl,re} \sim \varepsilon$ and $\tilde{Z}_{gdl,im} \sim \varepsilon$. In other words, as $\varepsilon \to 0$, the solid curve in Figure 7 gets closer to the Warburg's 45°–slope straight line. Physically, this means that with the decreasing reaction penetration depth, the system "porous electrode + GDL" tends to the system "planar electrode + GDL", which is described by the Warburg impedance. The frequency $\tilde{\omega}$, where the real part of the GDL impedance becomes negative immediately follows from Eq. 41:

$$\tilde{\omega} = \frac{1}{2\alpha}, \quad \text{or} \quad \omega = \omega^* = \frac{i_*}{C_{dl} b_1} \qquad [43]$$

Lower ε corresponds to higher i_*, i.e, with the decrease in ε, the frequency $\omega^* \to \infty$, Eq. 43. Note that negative $\tilde{Z}_{gdl,re}$ does not change the sign of the real part of the total system impedance Re $(\tilde{Z}_{ccl} + \tilde{Z}_{gdl})$. Calculations show that this real part remains positive for all system parameters.

Eqs. 41, 42 are valid provided that $\tilde{\omega}$ is sufficiently large, i.e., the ratio $\tilde{\omega}/\varepsilon^2$ must be large; these equations are not valid in the medium– and low frequency regions. Numerical calculations lead to a simple result for the summit frequencies of the ACL and the GDL arcs in the electrode spectrum (Figure 6):

$$\tilde{\omega}^*_{ccl} = \frac{1}{2\alpha}, \quad \text{or} \quad \omega^*_{ccl} = \frac{i_*}{C_{dl} b_1} \qquad [44]$$

$$\tilde{\omega}^*_{gdl} = \frac{2.54\varepsilon^2 \tilde{D}_b}{\mu^2 \tilde{l}_b^2}, \quad \text{or} \quad \omega^*_{gdl} = \frac{2.54 D_b}{l_b^2} \qquad [45]$$

In contrast to the large–ε electrode, here, the summit frequencies of the ACL and the GDL arcs are given by quite different equations, and these arcs are typically well separated. Eq. 45 has long been known for the finite–length Warburg impedance (Ref. 23, page 89). Thus, if an experimental spectrum is available, Eq. 45 gives the feed molecules (hydrogen) diffusion coefficient in the anode supporting layer. Note that the frequency 45 is independent of the feed molecules concentration. It is also worth noting that comparing Eqs. 43 and 44 we see, that the top of the ACL arc is achieved at the frequency, where the real part of the GDL impedance becomes negative.

PEMFC cathode and hydrogen crossover.—A feature of real PEMFCs is hydrogen crossover through the polymer membrane. The crossover turns the cathode operation into a regime with the virtual anode. This regime has been analyzed in detail for a direct methanol fuel cell cathode,[18] where methanol crossover leads to the same effects. Virtual anode means that a small part of the cathode thickness located at the membrane surface works as an anode, i.e., it converts incoming hydrogen molecules into protons. The conversion is extremely fast due to a very high polarization potential for the hydrogen oxidation on the cathode side. The rest part of the electrode thickness works as a normal cathode converting the proton current into electron current.

In PEM fuel cells, the characteristic current density of H_2 crossover is about several mA cm^{-2} (Ref. 13). It is easy to verify that at this current density, the cathode operates in the Tafel regime with the exponential dependence of current on the overpotential. In other words, a true OCP regime in a real PEMFC cannot be achieved due to hydrogen crossover.

In the Tafel regime, the static resistivity of the cathode is given by[21]

$$R^{\text{Tafel}}_{ccl} = \frac{l_t}{3\sigma_p} + \frac{b_1}{\alpha j_{cross}} \qquad [46]$$

where j_{cross} is the equivalent current density of crossover. Comparing this equation to the large–ε branch of Eq. 27 we see that instead of the the term $b_1/(i_* l_t)$, in Eq. 46 we get the term $b_1/(\alpha j_{cross})$. Typically, $j_{cross} \gg i_* l_t$, and hence in the quasi–OCP state, the static cell resistivity corresponds to the crossover current density.

Indeed, with $j_{cross} \simeq 1$ mA cm^{-2}, the second term in Eq. 46 greatly dominates. A typical Tafel slope of the ORR electrode is $b_1/\alpha = RT/(\alpha F) = 0.03$ V and from Eq. 46 we get $R^{\text{Tafel}}_{ccl} \simeq 30\ \Omega\ \text{cm}^2$. This agrees with the DC resistivity of $5.7 \cdot 4.4 \simeq 25\ \Omega\ \text{cm}^2$, which exhibits the spectrum in Figure 2.[34] Here, the factor 4.4 cm^2 is the cell active surface in Ref. 34.

It is worth noting that in the Tafel regime, the summit frequency (corresponding to the top of the faradaic arc) is given by[21]

$$\omega^*_{ccl} = \frac{\alpha j_{cross}}{C_{dl} b_1 l_t} \qquad [47]$$

Equations 46 and 47 can be used to calculate j_{cross} in the cell. Figure 3 shows the impedance spectra of a high–temperature PEM fuel cell measured at the quasi–OCP for different operating temperatures.[24] The static cell resistivity dramatically decreases with the temperature growth (Figure 3). The charge–transfer resistivity R_{ct} data reported in Ref. 24 and the transfer coefficient for the HT–PEMFC cathode $\alpha = 0.7$ (Refs. 20, 32) allow us to calculate j_{cross} in the cell, $j_{cross} \simeq b_1/(\alpha R_{ct})$ (Figure 8). As can be seen, in this temperature range, the crossover current linearly increases with the cell temperature. The range of crossover current densities in Figure 8 agrees with the measurements[28] for a similar cell.

As discussed above, the crossover current density is three orders of magnitude larger, than the ORR exchange current density; nonetheless, the GDL transport resistivity is three orders of magnitude less, than the CCL charge–transfer resistivity. This means, that even in the quasi–OCP state, the GDL impedance is masked by much larger CCL impedance, and no separate GDL arc is seen in Figure 2. Finally we note that the main result of this Section stems from comparison of Eqs. 46 and 27. Eq. 46 was reported in Ref. 21, while Eq. 27 seemingly has not been derived so far.

Conclusions

A model for the fuel cell impedance at open circuit potential is developed and analytical expressions for the impedance of the catalyst layer and the gas–diffusion layer are obtained. These impedances are connected in series. In general, the GDL transport impedance differs from the Warburg impedance.

A key parameter determining the relation between the CL and the GDL impedances is ε, Eq. 7. In PEMFCs, $\varepsilon \gg 1$, and the faradaic and GDL transport impedances merge. Furthermore, the GDL impedance appears to be six orders of magnitude smaller, than the CCL (faradaic) impedance, which makes the GDL impedance completely "invisible". In the anode of an anode–supported SOFC, the parameter ε is small, $\varepsilon \ll 1$, and the impedances of the anode catalyst layer and of the anode supporting layer (GDL) form well–separated arcs. Furthermore, in SOFC anode, the GDL transport impedance is close to the Warburg finite–length impedance.

In real PEMFCs, hydrogen crossover turns the cathode side into the Tafel regime of operation, i.e., a true OCP state in these cells cannot be achieved. The impedance spectra measured at zero current in the load correspond, in fact, to the crossover current density j_{cross} flowing in the cathode. These spectra can be used to calculate j_{cross}.

Appendix: GDL Impedance at Small ε

A formal Taylor series expansion for the general GDL impedance Eq. 22 over ε cannot be obtained by the standard procedure due to the terms of the form $\sin(y/\varepsilon)$, which rapidly oscillate as $\varepsilon \to 0$. However, the leading term of the expansion can be derived as following.

Separating the real and imaginary parts of Eq. 22, we come to

$$\tilde{Z}_{gdl,re} = \frac{\alpha(1+2\alpha\tilde{\omega})\varepsilon \sin(\xi)\cos(\xi)}{\mu\sqrt{\tilde{\omega}\tilde{D}_b}(1+4\alpha^2\tilde{\omega}^2)(\cosh^2\xi - \sin^2\xi)} + \frac{\alpha(1-2\alpha\tilde{\omega})\varepsilon \sinh(\xi)\cosh(\xi)}{\mu\sqrt{\tilde{\omega}\tilde{D}_b}(1+4\alpha^2\tilde{\omega}^2)(\cosh^2\xi - \sin^2\xi)} \quad [A1]$$

$$\tilde{Z}_{gdl,im} = \frac{\alpha(1-2\alpha\tilde{\omega})\varepsilon \sin(\xi)\cos(\xi)}{\mu\sqrt{\tilde{\omega}\tilde{D}_b}(1+4\alpha^2\tilde{\omega}^2)(\cosh^2\xi - \sin^2\xi)} - \frac{\alpha(1+2\alpha\tilde{\omega})\varepsilon \sinh(\xi)\cosh(\xi)}{\mu\sqrt{\tilde{\omega}\tilde{D}_b}(1+4\alpha^2\tilde{\omega}^2)(\cosh^2\xi - \sin^2\xi)} \quad [A2]$$

where

$$\xi = \frac{\mu\tilde{l}_b\sqrt{\tilde{\omega}}}{\varepsilon\sqrt{2\tilde{D}_b}} \quad [A3]$$

From Eq. A3 it follows, that for $\varepsilon \to 0$ and sufficiently large $\tilde{\omega}$, we have $\xi \to \infty$. The first terms on the right side of Eqs. A1 and A2 contain trigonometric functions of ξ in the numerator, and a single hyperbolic $\cosh\xi$ in the denominator. Thus, these terms vanish as $\xi \to \infty$. In the denominator of the second terms on the right side of Eqs. A1 and A2 we can neglect $\sin^2(\xi)$ as compared to the exponentially growing hyperbolic $\cosh^2(\xi)$. Further, for $\xi \to \infty$, we have $\sinh\xi \simeq \cosh\xi \simeq \exp(\xi)/2$, which finally leads to Eqs. 41 and 42.

List of Symbols

~	Marks dimensionless variables
b_1	Characteristic potential $b_1 = RT/F$, V
C_{dl}	Double layer volumetric capacitance, F cm^{-3}
c, c_{ox}	Oxygen molar concentration in the CCL, mol cm^{-3}
c_b	Oxygen molar concentration in the GDL, mol cm^{-3}
c^{ref}	Oxygen molar concentration in the channel, mol cm^{-3}
D_b	Effective oxygen diffusion coefficient in the GDL, cm^2 s^{-1}
F	Faraday constant, C mol^{-1}
f	Regular frequency, Hz
j_0	Local cell current density, A cm^{-2}
i	Imaginary unit
i_*	Volumetric exchange current density, A cm^{-3}
l_b	Gas–diffusion layer thickness, cm
l_t	Catalyst layer thickness, cm
R_{ccl}	Static differential resistivity of the CCL, Ω cm^2
R_{gdl}	Static differential resistivity of the GDL, Ω cm^2
t	Time, s
t_*	Characteristic time of double layer charging, s, Eq. 4
x	Coordinate through the cell, cm
Z	Total impedance of the cathode side, Ω cm^2
Z_{ccl}	CCL impedance, Ω cm^2
Z_{gdl}	GDL impedance, Ω cm^2

Greek

α	Transfer coefficient
ε	Newman's dimensionless reaction penetration depth, Eq. 7
η	ORR overpotential (positive by convention), V
κ	Dimensionless parameter, Eq. 6
μ	Dimensionless parameter, Eq. 12
ξ	Dimensionless parameter, Eq. A3
σ_p	CCL ionic conductivity, Ω^{-1} cm^{-1}
ϕ	Dimensionless parameter, Eq. 18
ω	Angular frequency ($\omega = 2\pi f$), s^{-1}
ω^*	Characteristic angular frequency, s^{-1}, Eq. 31

Subscripts

0	Membrane/CCL interface
1	CCL/GDL interface
b	GDL
ccl	CCL
gdl	GDL
t	Catalyst layer
∗	Characteristic value

Superscripts

0	Steady–state value
1	Small–amplitude perturbation
in	Oxygen channel inlet

References

1. S. Arisetty, X. Wang, R. K. Ahluwalia, R. Mukundan, R. Borup, J. Davey, D. Langlois, F. Gambini, O. Polevaya, and S. Blanchet, "Catalyst durability in PEM fuel cells with low platinum loading," *J. Electrochem. Soc.*, **159**, B455 (2012).
2. C. Bao and W. G. Bessler, "Two–dimensional modeling of a polymer electrolyte membrane fuel cell with long flow channel. Part ii. physics–based electrochemical impedance analysis," *J. Power Sources*, **278**, 675 (2015).
3. R. Barfod, M. Mogensen, T. Klemensø, A. Hagen, Y.-L. Liu, and P. V. Hendriksen, "Detailed characterization of anode–supported SOFCs by impedance spectroscopy," *J. Electrochem. Soc.*, **154**, B371 (2007).
4. Y. Bultel, L. Genies, O. Antoine, P. Ozil, and R. Durand, "Modeling impedance diagrams of active layers in gas diffusion electrodes: Diffusion, ohmic drop effects and multistep reactions," *J. Electroanal. Chem.*, **527**, 143 (2002).
5. Y. Bultel, K. Wiezell, F. Jaouen, P. Ozil, and G. Lindbergh, "Investigation of mass transport in gas diffusion layer at the air cathode of a PEMFC," *Electrochimica Acta*, **51**, 474 (2005).
6. M. Cimenti, D. Bessarabov, M. Tam, and J. Stumper, "Investigation of proton transport in the catalyst layer of PEM fuel cells by electrochemical impedance spectroscopy," *ECS Transactions*, **28**(23), 147 (2010).
7. M. Eikerling and A. A. Kornyshev, "Electrochemical impedance of the cathode catalyst layer in polymer electrolyte fuel cells," *J. Electroanal. Chem.*, **475**, 107 (1999).
8. M. Eikerling and A. A. Kulikovsky, *Polymer Electrolyte Fuel Cells: Physical Principles of Materials and Operation*. CRC Press, London, 2014.
9. A. A. Franco, P. Schott, C. Jallut, and B. Maschke, "A multi-scale dynamic mechanistic model for the transient analysis of PEFCs," *Fuel Cells*, **7**, 99 (2007).
10. Y. Fu, Y. Jiang, S. Poizeau, A. Dutta, A. Mohanram, J. D. Pietras, and M. Z. Bazant, "Multicomponent gas diffusion in porous electrodes," *J. Electrochem. Soc.*, **162**, F613 (2015).
11. D. Gerteisen, A. Hakenjos, and J. O. Schumacher, "AC impedance modeling study on porous electrodes of proton exchange membrane fuel cells using an agglomerate model," *J. Power Sources*, **173**, 346 (2007).
12. Q. Guo and R. E. White, "A steady–state impedance model for a PEMFC cahode," *J. Electrochem. Soc.*, **151**, E133 (2004).
13. M. Inaba, T. Kinumoto, M. Kiriake, R. Umebayashi, A. Tasaka, and Z. Ogumi, "Gas crossover and membrane degradation in polymer electrolyte fuel cells," *Electrochimica Acta*, **51**, 5746 (2006).

14. F. Jaouen and G. Lindbergh, "Transient techniques for investigating mass–transport limitations in gas diffusion electrode," *J. Electrochem. Soc.*, **150**, A1699 (2003).
15. M. S. Kondratenko, M. O. Gallyamov, and A. R. Khokhlov, "Performance of high temperature fuel cells with different types of PBI membranes as analyzed by impedance spectroscopy," *Int. J. Hydrogen Energy*, **37**, 2596 (2012).
16. A. Kulikovsky and O. Shamardina, "A model for PEM fuel cell impedance: Oxygen flow in the channel triggers spatial and frequency oscillations of the local impedance," *J. Electrochem. Soc.*, 162, F1068 (2015).
17. A. A. Kulikovsky, "A physical model for the catalyst layer impedance," *J. Electroanal. Chem.*, **669**, 28 (2012).
18. A. A. Kulikovsky, "A model for DMFC cathode performance," *J. Electrochem. Soc.*, **159**, F644 (2012).
19. A. A. Kulikovsky, "Exact low–current analytical solution for impedance of the cathode catalyst layer in a PEM fuel cell," *Electrochimica Acta*, **147**, 773 (2014).
20. A. A. Kulikovsky, "One-dimensional impedance of the cathode side of a PEM fuel cell: Exact analytical solution," *J. Electrochem. Soc.*, **162**, F217 (2015).
21. A. A. Kulikovsky and M. Eikerling, "Analytical solutions for impedance of the cathode catalyst layer in PEM fuel cell: Layer parameters from impedance spectrum without fitting," *J. Electroanal. Chem.*, **691**, 13 (2013).
22. A. Lasia, *Electrochemical Impedance Spectroscopy and its Applications*. Springer, New York, 2014.
23. J. R. Macdonald, *Impedance Spectroscopy*. Wiley, New York, 1987.
24. W. Maier, T. Arlt, K. Wippermann, C. Wannek, I. Manke, W. Lehnert, and D. Stolten, "Correlation of synchrotron X-ray radiography and electrochemical impedance spectroscopy for the investigation of HT-PEFCs," *J. Electrochem. Soc.*, **159**, F398 (2012).
25. J. Mainka, G. Maranzana, A. Thomas, J. Dillet, S. Didierjean, and O. Lottin, "One-dimensional model of oxygen transport impedance accounting for convection perpendicular to the electrode," *Fuel Cells*, **12**, 848 (2012).
26. A. C. Okafor and H.-M. C. Mogbo, "Investigation of the effects of catalyst loading and gas flow rate on polymer electrolyte membrane (PEM) fuel cell performance and degradation," *J. Fuel Cell Sci. Techn.*, **9**, 011006 (2012).
27. M. E. Orazem and B. Tribollet, *Electrochemical Impedance Spectroscopy*. Wiley, New–York, 2008.
28. J. Park, L. Wang, S. G. Advani, and A. K. Prasad, "Mechanical stability of H_3PO_4–doped PBI/hydrophilic–pretreated PTFE membranes for high temperature PEMFCs," *Electrochimica Acta*, **120**, 30 (2014).
29. S. Primdahl and M. Mogensen, "Gas diffusion impedance in characterization of solid oxide fuel cell anodes," *J. Electrochem. Soc.*, **146**, 2827 (1999).
30. I. A. Schneider, M. H. Bayer, and S. von Dahlen, "Locally resolved electrochemical impedance spectroscopy in channel and land areas of a differential polymer electrolyte fuel cell," *J. Electrochem. Soc.*, **158**, B343 (2011).
31. B. P. Setzler and Th. F. Fuller, "A physics–based impedance model of proton exchange membrane fuel cells exhibiting low–frequency inductive loops," *J. Electrochem. Soc.*, **162**, F519 (2015).
32. O. Shamardina, M. S. Kondratenko, A. V. Chertovich, and A. A. Kulikovsky, "A simple transient model for a high temperature PEM fuel cell impedance," *Int. J. Hydrogen Energy*, **39**, 2224 (2014).
33. Y. Shi, N. Cai, C. Li, C. Bao, E. Croiset, J. Qian, Q. Hu, and S. Wang, "Simulation of electrochemical impedance spectra of solid oxide fuel cells using transient physical models," *J. Electrochem. Soc.*, **155**, B270 (2008).
34. C. Song, Y. Tang, J. L. Zhang, J. Zhang, H. Wang, J. Shen, S. McDermid, J. Li, and P. Kozak, "PEM fuel cell reaction kinetics in the temperature range of 23-120 °c," *Electrochimica Acta*, **52**, 2552 (2007).
35. T. E. Springer, T. A. Zawodzinski, M. S. Wilson, and S. Gottesfeld, "Characterization of polymer electrolyte fuel cells using AC impedance spectroscopy," *J. Electrochem. Soc.*, **143**, 587 (1996).
36. J. R. Vang, S. J. Andreasen, and S. K. Kaer, "A transient fuel cell model to simulate HTPEM fuel cell impedance spectra," *J. Fuel Cell Sci. Techn.*, **9**, 021005 (2012).
37. P. C. Wu, H. S. Jheng, and S. S. Shy, "Electrochemical impedance measurement and analysis of anodic concentration polarization for pressurized solid oxide fuel cells," *J. Electrochem. Soc.*, **161**, F513 (2014).
38. H. Zhu and R. J. Kee, "Modeling distributed charge–transfer processes in SOFC membrane–electrode assemblies," *J. Electrochem. Soc.*, **155**, B715 (2008).